ELSEVIER

Solid State Nuclear Magnetic Resonance 14 (1999) 43–58

SOLID STATE
Nuclear Magnetic
Resonance

Multiple-quantum relaxation in the magic-angle-spinning NMR of ^{13}C spin pairs

T. Karlsson [a], A. Brinkmann [a], P.J.E. Verdegem [a,b], J. Lugtenburg [b], M.H. Levitt [a,*]

[a] *Division of Physical Chemistry, Arrhenius Laboratory, Stockholm University, S-106 91 Stockholm, Sweden*
[b] *Leiden Institute of Chemistry, Rijksuniversiteit Leiden, NL-2300 RA Leiden, Netherlands*

Received 20 January 1999; accepted 10 March 1999

Abstract

We determine the decay rate constants of zero-, double- and single-quantum coherence for ^{13}C spin pairs in magic-angle-spinning solid-state NMR. The double-quantum coherence is excited by a C7 pulse sequence and converted into zero-quantum coherence by a frequency-selective pair of $\pi/2$ pulses. The zero-quantum coherence is reconverted into observable magnetization by a second pair of $\pi/2$ pulses followed by a second C7 sequence. In a magnetically dilute system where the ^{13}C–^{13}C distance is 0.296 nm, the relaxation rate constants are consistent with a model of uncorrelated random fields at the two labeled ^{13}C sites. In a fully-labelled system with a short ^{13}C–^{13}C distance of 0.153 nm, the measured rate constants are inconsistent with the uncorrelated random field model.

Keywords: Multiple-quantum coherence; Double-quantum coherence; Zero-quantum coherence; C7; Magic-angle spinning

1. Introduction

Solid state NMR is commonly used to investigate the molecular structure and conformation of organic molecules, through the determination of internuclear distances [1–7] and molecular torsion angles [7–14]. Many of these studies exploit samples containing pairs of ^{13}C nuclei, introduced by chemical means at the molecular sites of interest.

Many NMR tools for determining molecular structure exploit multiple quantum coherence in the ensemble of $^{13}C_2$ spin pairs. For example, rotational resonance [15–18] estimates internuclear distances by transferring magnetization between the spin sites through an intermediate state of zero-quantum coherence. Double-quantum coherence is exploited in experiments for estimating molecular torsion angles [8–13]. These methods have been applied to large molecular systems including membrane proteins [1,7,11].

Given the important role of multiple-quantum $^{13}C_2$ coherence in molecular structural studies, it is important to investigate the factors leading to the decay of these coherences. In particular, the measurement of internuclear distances by rotational resonance NMR requires an estimate of the decay time constant T_2^{ZQ} of the $^{13}C_2$ zero-quantum coherence [17].

Until recently, there have been few direct experimental studies of coherence decay in the solid state NMR of $^{13}C_2$ spin pairs. The estimate of T_2^{ZQ} in

* Corresponding author: Fax: +46-8-152187; E-mail: mhl@physc.su.se

0926-2040/99/$ - see front matter
PII: S0926-2040(99)00008-9

rotational resonance studies has generally relied on measuring the single-quantum relaxation rate constants through linewidth estimates, and then extending these results to the zero-quantum case by invoking a simple relaxation model [17].

The uncorrelated random field model (URF model) is widely used for this purpose [19]. In this model, each of the ^{13}C sites is considered to experience a rapid, fluctuating random field. The fluctuations of the fields at the two sites are considered to be completely uncorrelated. If the random field fluctuations are sufficiently fast, this model predicts exponential decay of all the spin coherences, and a simple relationship between the coherence decay rate constants. If the two spins are denoted S_j and S_k, then the coherence decay rate constants are related through

$$R_j^{SQ} + R_k^{SQ} = R^{ZQ} = R^{DQ} \quad (1)$$

where R_j^{SQ} is the decay rate constant for single quantum coherence of spin j, and similarly for R_k^{SQ}. R^{ZQ} and R^{DQ} are the decay rate constants for zero-quantum and double-quantum coherences in the spin-pair ensemble. These rate constants are defined as the inverse of the corresponding transverse relaxation time constants, i.e., $R^{ZQ} = 1/T_2^{ZQ}$, $R^{DQ} = 1/T_2^{DQ}$, $R_j^{SQ} = 1/T_{2j}^{SQ}$ and $R_k^{SQ} = 1/T_{2k}^{SQ}$.

Normally, magic-angle-spinning (MAS) is used to enhance the resolution and sensitivity of the ^{13}C spectrum by averaging out chemical shift anisotropies [20]. In addition, strong proton decoupling is applied in order to eliminate the influence of heteronuclear ^1H–^{13}C dipolar couplings. For magnetically-isolated spin pairs, the main mechanism of ^{13}C coherence decay is usually incomplete suppression of the heteronuclear ^{13}C–^1H couplings by the rf decoupling field and the magic-angle sample rotation [21]. If the ^{13}C spin pairs are not magnetically isolated from each other, homonuclear dipole–dipole couplings between ^{13}C spins on different molecules also contribute to the coherence decay.

The applicability of the URF model in these circumstances has not been tested directly. The case of multiple-quantum relaxation for ^{13}C spins separated by long distances is of particular relevance, since the determination of internuclear distances requires an estimate of the zero-quantum decay time constant T_2^{ZQ}.

In this paper, we present direct experimental measurements of double-quantum, zero-quantum and single-quantum decay rate constants for $^{13}C_2$ spin pairs in MAS solids. We test the validity of Eq. (1) and hence the applicability of the URF model.

We present experimental results on two different molecular systems, 10%-[11,20-$^{13}C_2$]-all-*E*-retinal and 98%-[$^{13}C_2$,^{15}N]-glycine (see Fig. 1 and Section 5). In the retinal sample, the $^{13}C_2$ internuclear distance is 0.296 nm and the spins are well isolated by isotopic dilution. In the glycine sample, the $^{13}C_2$ internuclear distance is 0.153 nm, and there are significant intermolecular spin–spin interactions.

^{15}N labeling was used in the glycine sample to avoid complications caused by dipolar couplings between the ^{13}C spins and the quadrupolar ^{14}N nuclei [22]. The heteronuclear ^{13}C–^{15}N dipolar coupling is relatively small. Since the ^{15}N nuclei have spin = 1/2 and long spin lattice relaxation time constants, the ^{15}N spins do not give rise to appreciable broadening of the ^{13}C signals in the presence of MAS. The ^{15}N spins are ignored in the following discussion.

In the case of 10%-[11,20-$^{13}C_2$]-retinal, we find that the measured decay rate constants of zero-quantum and double-quantum coherence are very similar. This is consistent with the URF model. The experimental single-quantum decay rate constants are also qualitatively consistent with the URF model.

In the case of 98%-[$^{13}C_2$,^{15}N]-glycine, on the other hand, the measured decay rate constant for the

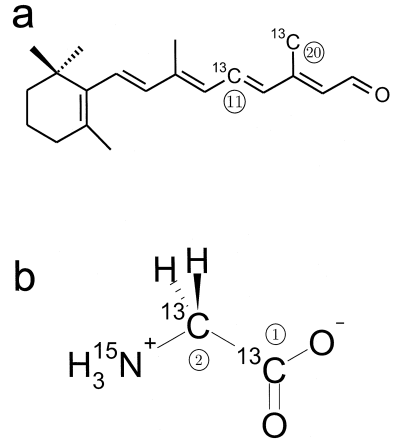

Fig. 1. Selectively labeled molecules used in this study: (a) [11,20-$^{13}C_2$]-all-*E*-retinal and (b) [$^{13}C_2$,^{15}N]-glycine. The site labels are indicated by circled numbers.

zero-quantum coherence is much smaller than the rate constant for the double-quantum decay. The experimental single-quantum decay constants are also inconsistent with the URF model. These discrepancies may be due to the short ^{13}C–^{13}C distance in this compound, and also the effect of intermolecular ^{13}C–^{13}C interactions.

2. Double quantum experiments

2.1. Pulse sequences

Double-quantum $^{13}C_2$ coherence was investigated by the pulse sequences depicted in Fig. 2.

The row marked *I* denotes the rf-fields applied at the Larmor frequency of the abundant protons, while *S* denotes the rf-fields applied at the ^{13}C Larmor frequency (rows a and b). The diagrams also show

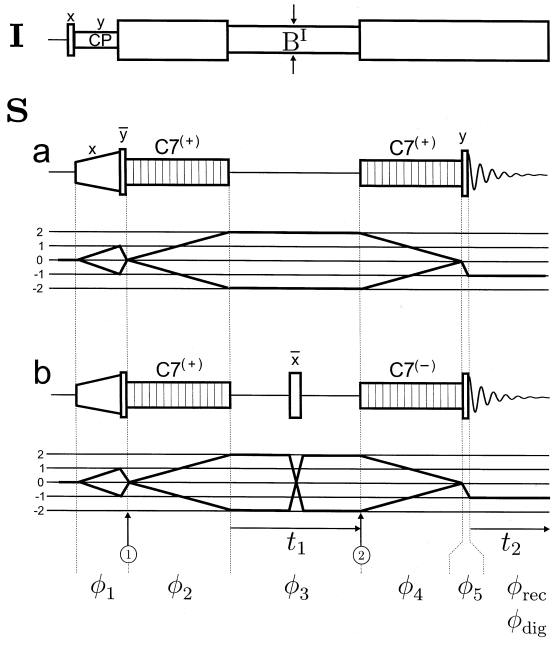

Fig. 2. Pulse sequences for the observation of double-quantum spin dynamics together with coherence transfer pathway diagrams. In (a), double-quantum coherence is excited by a C7-sequence and evolves freely under the incrementable delay t_1. In (b), the double-quantum evolution period t_1 is interrupted by a strong π-pulse, which refocuses chemical shifts and magnetic field inhomogeneities. The sequences $C7^{(+)}$ and $C7^{(-)}$ are described in the text.

the desired coherence transfer pathways [23] (CTPs) for the *S*-spins. The overall phases of the pulse sequence blocks are denoted $\phi_1 \ldots \phi_5$. The rf receiver phase is denoted ϕ_{rec}, and the post-digitization phase ϕ_{dig} [29]. These phases are cycled between different acquired transients, in order to select signals from the desired CTP.

All sequences start with ramped cross-polarization to enhance the transverse *S*-spin magnetization [24,25]. The following $\pi/2$-pulse converts the transverse magnetization into longitudinal *S*-spin magnetization.

The C7 sequence, as described in Ref. [26], converts the *S*-spin longitudinal magnetization into (± 2)-quantum coherence, as indicated in the CTP-diagram. After an evolution period t_1, the double-quantum coherences are reconverted into observable magnetization by a second C7 sequence, followed by a $\pi/2$ pulse. In Fig. 2b, a π pulse is inserted at the centre of the double-quantum evolution period, in order to compensate for magnetic field inhomogeneities (see below).

The C7 sequence consist of a set of rf-cycles C_ϕ, each with a duration equal to $\tau_C = 2\tau_r/7$, where $\tau_r = |2\pi/\omega_r|$ is the rotation period, and ω_r is the sample rotation frequency. The index ϕ denotes the overall phase of the cycle C_ϕ. In the experiments described here, each cycle consists of two phase-shifted pulses, both with a flip angle of 2π, i.e., $C_\phi = (2\pi)_\phi(2\pi)_{\phi+\pi}$ in conventional pulse sequence notation. Other compositions of the C_ϕ-cycle are also possible [27,28].

Two different types of C7-sequences are used, denoted $C7^{(+)}$ and $C7^{(-)}$ in Fig. 2. In the sequence $C7^{(+)}$, the phase is *incremented* in steps of $2\pi/7$ between cycles, i.e., $C7_\Phi^{(+)} = C_\Phi C_{\Phi+2\pi/7} C_{\Phi+4\pi/7} \ldots C_{\Phi+2\pi(q-1)/7}$, where q is the total number of cycles in the block. Here Φ is the overall phase of the $C7^{(+)}$ sequence. The total duration of the C7 block is $q\tau_C$. In the sequence $C7^{(-)}$, on the other hand, the phase is *decremented* in steps of $2\pi/7$ between cycles, i.e., $C7_\Phi^{(-)} = C_\Phi C_{\Phi-2\pi/7} C_{\Phi-4\pi/7} \ldots C_{\Phi-2\pi(q-1)/7}$.

2.2. Double quantum excitation

Suppose the sample contains pairs of ^{13}C sites, denoted *j* and *k*. The isotropic chemical shifts of the

sites are ordered such that $\delta_j^{iso} < \delta_k^{iso}$. The ^{13}C spins in the two sites are denoted S_j and S_k. The through space dipole–dipole coupling between the spins is given by

$$b_{jk} = -\left(\frac{\mu_0}{4\pi}\right)\frac{\gamma_j\gamma_k\hbar}{r_{jk}^3} \tag{2}$$

in rad s^{-1}, where r_{jk} is the internuclear distance between site j and site k. The signs of frequency and phases are treated as in Ref. [29].

The average Hamiltonian for the $C7^{(+)}$ sequence, as discussed in Ref. [26], is given by

$$\bar{H}_{C7}^{(+)}\left(t_0,\Phi,\Omega^{MR}\right) \simeq \left|\omega_{C7}^{(+)}\right|\frac{1}{2}\left\{e^{+i\phi_{C7}^{(+)}}S_j^-S_k^- + e^{-i\phi_{C7}^{(+)}}S_j^+S_k^+\right\} \tag{3}$$

where the double-quantum nutation frequency and nutation phase angle during $C7^{(+)}$ are equal to

$$\left|\omega_{C7}^{(+)}\right| = \frac{343\left(1+\sin(\pi/14)\right)^{1/2}}{520\pi}b_{jk}\sin\left(2\beta^{MR}\right) \tag{4}$$

$$\phi_{C7}^{(+)}\left(t_0,\Phi,\gamma^{MR}\right) = -\tan^{-1}\left(\frac{1+\sin(\pi/14)}{\cos(\pi/14)}\right) - \omega_r t_0 + \gamma^{MR} + 2\Phi \tag{5}$$

Here t_0 is the starting timepoint of the $C7^{(+)}$ sequence, Φ is the overall rf phase of the sequence, and $\Omega^{MR} = \{\alpha^{MR},\beta^{MR},\gamma^{MR}\}$ represents the Euler angles defining the relative orientation of the molecular reference frame M and the rotor-fixed frame R. The z-axis of frame M is defined to be colinear with the internuclear vector between sites S_j and S_k. The Euler angles are random variables in a powdered solid. Note that only the phase of the nutation axis depends on the Euler angle γ^{MR}. This feature is partly responsible for the good performance of C7 in a powder [26–28].

When two $C7^{(+)}$ sequences are combined, as in Fig. 2a, it is important to ensure that the nutation axis phases $\phi_{C7}^{(+)}$ are consistent between the two sequences, independent of the time interval between them. Suppose that the first $C7^{(+)}$ sequence starts at timepoint $t_{①}$ (marked in Fig. 2), and has rf phase ϕ_2, while the second $C7^{(+)}$ sequence starts at time point $t_{②}$, and has rf phase ϕ_4. Compatible nutation axis phases are ensured by adjusting the rf phases to satisfy

$$\omega_r t_{①} - 2\phi_2 = \omega_r t_{②} - 2\phi_4 + N\pi \tag{6}$$

where N is an integer. The sign of the signal is inverted in sign if N is even. This equation requires that the rf phase difference between the two $C7^{(+)}$ sequences is linearly proportional to the time interval between the sequences.

The sequence $C7^{(-)}$ has a different average Hamiltonian, given by

$$\bar{H}_{C7}^{(-)}\left(t_0,\Phi,\Omega^{MR}\right) \simeq \left|\omega_{C7}^{(-)}\right|\frac{1}{2}\left\{e^{+i\phi_{C7}^{(-)}}S_j^-S_k^- + e^{-i\phi^{(-)}C7}S_j^+S_k^+\right\} \tag{7}$$

with

$$\left|\omega_{C7}^{(-)}\right| = \left|\omega_{C7}^{(+)}\right| \tag{8}$$

$$\phi_{C7}^{(-)}\left(t_0,\Phi,\gamma^{MR}\right) = \tan^{-1}\left(\frac{1+\sin(\pi/14)}{\cos(\pi/14)}\right) + \omega_r t_0 - \gamma^{MR} + 2\Phi \tag{9}$$

where t_0 is the initial timepoint and Φ is the rf phase. The $C7^{(-)}$ sequence is not directly compatible with the $C7^{(+)}$ sequence, since the nutation axis phases both depend on the orientational angle γ^{MR}, but with opposite signs. As a result, combination of a $C7^{(+)}$ sequence with a $C7^{(-)}$ sequence leads to destruction of the double-quantum filtered signal in a powder [30].

However, if a π pulse is inserted between the $C7^{(+)}$ and $C7^{(-)}$ sequences, as in Fig. 2b, the two sequences become compatible, provided that the rf phases are adjusted to satisfy

$$\omega_r t_{①} - 2\phi_2 + 4\phi_3 = \omega_r t_{②} + 2\phi_4 + N\pi \tag{10}$$

where N is an integer, and ϕ_3 is the phase of the π pulse (see Fig. 2). The signal is inverted if N is odd. The phase-compatibility and phase–time relationships for C7 sequences are discussed in more detail elsewhere [30].

2.3. Double quantum spectrum

The pulse sequence in Fig. 2a may be used to obtain the two-dimensional double-quantum spectrum, as demonstrated previously in ^{31}P NMR [31].

Fig. 3 shows a two-dimensional spectrum obtained by the pulse sequence in Fig. 2a for [$^{13}C_2$,^{15}N]-glycine. The spinning frequency was 5.000 kHz, and the decoupler level B^I during t_1 corresponded to a proton nutation frequency $\omega^I_{nut}/2\pi = 90$ kHz. A complex FT was applied in the t_2-dimension, and a cosine FT in the t_1-dimension.

We observe two single quantum peaks in the ω_2-dimension, corresponding to the two ^{13}C chemical sites in glycine, and a single narrow peak in the ω_1-dimension corresponding to double-quantum coherence. The small peak at $\omega_2/2\pi \simeq 1.6$ kHz is a spinning sideband.

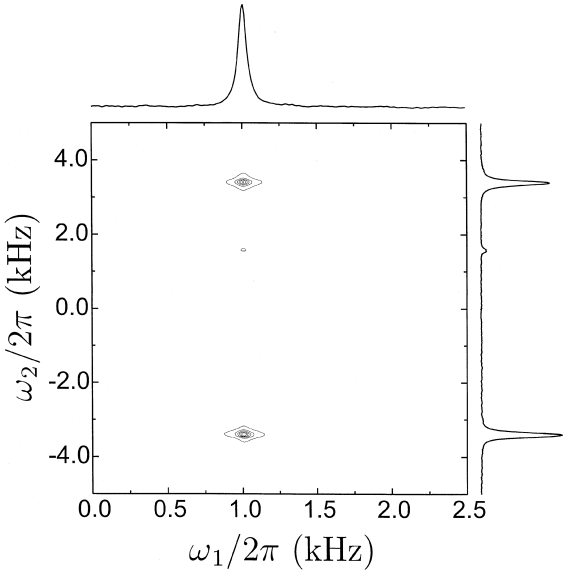

Fig. 3. Two-dimensional spectrum obtained by the pulse sequence in Fig. 2a on [$^{13}C_2$,^{15}N]-glycine. The single-quantum dimension is ω_2, and the double-quantum dimension is ω_1. The line graphs are projections of the signal-containing regions onto the frequency axes. The double-quantum peak appears at $\omega_1/2\pi = 1.000$ kHz and has a width at half height of $\simeq 70$ Hz.

The position of the double-quantum peak reflects evolution under the sum of isotropic chemical shifts, and is equal to

$$\omega^{DQ} = \omega_j^{iso} + \omega_k^{iso} \tag{11}$$

where ω_j^{iso} and ω_k^{iso} are the isotropic shift frequencies for spins j and k, respectively, both specified relative to the spectrometer reference frequency. To obtain a non-ambiguous double-quantum peak, the spectrometer reference frequency during t_1 was shifted by 500 Hz from the mean of the two isotropic chemical shift frequencies. The theoretical double-quantum frequency is then $\omega^{DQ}/2\pi \simeq 1.000$ kHz, which is well reproduced in the experiment.

The phases of the pulse sequence blocks ϕ_1, $\phi_2 \ldots \phi_5$ and the rf receiver phase ϕ_{rec} were cycled according to

$$\phi_1 = \frac{2\pi m}{n_1} + \phi_1^0$$

$$\phi_p = \frac{2\pi}{n_p}\,\mathrm{floor}\left(\frac{m}{n_1 n_2 \ldots n_{p-1}}\right) + \phi_p^0, \ (\text{for } p > 1)$$

$$\phi_{rec} = 0 \tag{12}$$

where the function floor(x) returns the largest integer not greater than x. Here ϕ_p^0 is the initial phase of the pulse sequence block ϕ_p, and m is the transient counter, $m = 0,1 \ldots n_{tot} - 1$, where n_{tot} is the number of transients in a complete phase cycle, $n_1 n_2 \ldots n_5 n_{rec}$. In the present case, the cycling parameters were $n_1 = 1$, $n_2 = 1$, $n_3 = 1$, $n_4 = 4$, $n_5 = 4$, $n_{rec} = 1$, $n_{tot} = 16$. On each transient, the post digitization phase ϕ_{dig} was adjusted to satisfy the equation

$$2\phi_2 - 2\phi_4 - \phi_5 + \phi_{rec} + \phi_{dig} = 2\phi_2^0 - 2\phi_4^0 - \phi_5^0 \tag{13}$$

This phase cycle selects (± 2)-quantum coherence during the evolution interval t_1.

The initial phases of the pulse sequence blocks were selected according to

$$\phi_1^0 = \phi_2^0 = \phi_3^0 = \phi_5^0 = 0 \tag{14}$$

$$\phi_4^0 = \frac{1}{2}\omega_r\left(t_{②} - t_{①}\right) + \frac{\pi}{2} \tag{15}$$

where $t_{①}$ and $t_{②}$ are the initial timepoints of the two C7 sequences (see Fig. 2). Note that this re-

quires the phase of the second C7 block to be linked dynamically to the interval between the two C7 sequences. This phase–time relationship is consistent with Eq. (6), and allows incrementation of the evolution interval t_1 in arbitrary time steps.

The experimental spectrum in Fig. 3 reveal a strong and narrow double-quantum peak, but cannot be used for an estimate of R^{DQ}, since the double-quantum decay contains contributions from inhomogeneous magnetic fields and chemical shift dispersion.

2.4. Decay of double quantum coherence

In the pulse sequence of Fig. 2b, a π-pulse is inserted in the free precession interval t_1 in order to refocus magnetic field inhomogeneities and chemical shifts. This sequence allows a reliable estimation of the homogeneous double-quantum decay rate constant R^{DQ}.

Phase cycling of the pulse sequence blocks is used in order to select (± 2)-quantum coherences during the evolution interval t_1. A suitable phase cycle is specified by Eq. (12), with $n_1 = 1$, $n_2 = 1$, $n_3 = 8$, $n_4 = 4$, $n_5 = 1$, $n_{rec} = 1$, $n_{tot} = 32$. On each transient, the post digitization phase ϕ_{dig} is adjusted to satisfy the equation

$$2\phi_2 - 4\phi_3 + 2\phi_4 - \phi_5 + \phi_{rec} + \phi_{dig} = 2\phi_2^0 - 4\phi_3^0 + 2\phi_4^0 - \phi_5^0 \quad (16)$$

where the initial phases are

$$\phi_1^0 = \phi_2^0 = \phi_3^0 = \phi_5^0 = 0 \quad (17)$$

$$\phi_4^0 = -\frac{1}{2}\omega_r \left(t_{②} - t_{①}\right) + \frac{\pi}{2} \quad (18)$$

The initial timepoints $t_{①}$ and $t_{②}$ are indicated in Fig. 2. This link between the pulse sequence timings and phases is compatible with Eq. (10) and allows the evolution interval t_1 to be incremented in arbitrary steps, without loss of double-quantum filtered signal.

2.4.1. 11,20-$^{13}C_2$-all-E-retinal

Fig. 4a shows experimental measurements of double-quantum decay in [11,20-$^{13}C_2$]-all-*E*-retinal (circles), together with the best fit to an exponential decay model (solid line). The symbols represent the sum of the two peak integrals in the single-quantum spectrum, as a function of the evolution interval t_1.

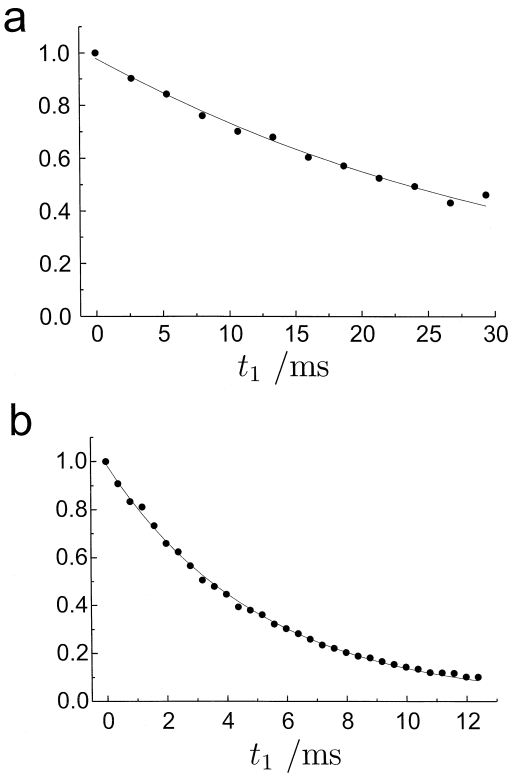

Fig. 4. Double quantum decays obtained by the pulse sequence in Fig. 2b on (a) [11,20-$^{13}C_2$]-all-*E*-retinal and (b) [$^{13}C_2$,^{15}N]-glycine. The points denote the sum of the integrated areas under the two spectral peaks as a function of evolution interval t_1. The curves were normalized so that the point at $t_1 = 0$ was equal to 1.0. In each case, the solid line is the best fit to an exponential decay.

The experiments were performed at a decoupler level B^I corresponding to a proton nutation frequency of 90 kHz, and a sample rotation frequency of 4.500 kHz.

A rather slow damping of double-quantum coherence is observed, which is described well by an exponential decay model. The estimated decay rate constant is $R^{DQ} = 29 \pm 2\ s^{-1}$ which corresponds to a relaxation time constant of $T_2^{DQ} = 35 \pm 2$ ms.

2.4.2. [$^{13}C_2$,^{15}N]-glycine

Fig. 4b shows results for [$^{13}C_2$,^{15}N]-glycine. The experiments were performed at a decoupler level B^I

corresponding to a proton nutation frequency of 90 kHz, and a sample rotation frequency of 5.000 kHz.

In this case a rather fast decay of the double-quantum coherence is observed. The data are well described by a decay rate constant $R^{DQ} = 197 \pm 3$ s^{-1} which corresponds to a relaxation time constant of $T_2^{DQ} = 5.09 \pm 0.05$ ms.

3. Zero-quantum experiments

3.1. Zero-quantum excitation

There are a number of methods for zero-quantum excitation in MAS NMR, such as exploiting rotational resonance [17,18], or by using rotor synchronized multiple-pulse sequences which generate a zero-quantum average dipolar Hamiltonian [32].

In this study, C7 is used to excite double-quantum coherence, which is then converted into zero-quantum coherence by a second pulse sequence. The reconversion of zero-quantum coherence into observable magnetization is carried out by reversing the process, again using an intermediate double-quantum state.

The appropriate pulse sequences are shown in Fig. 5. The sequence $C7^{(+)}$ is followed by two

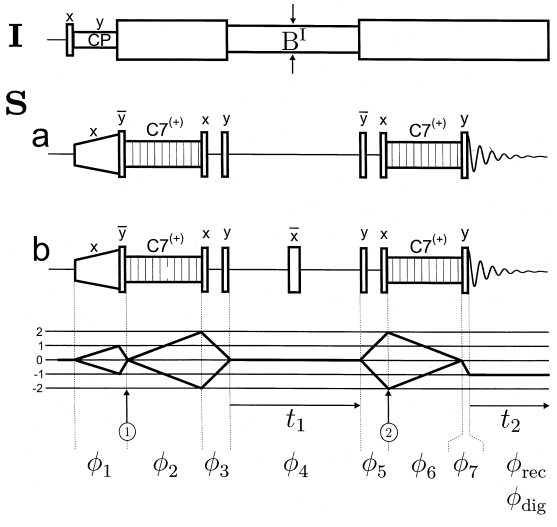

Fig. 5. Pulse sequences for the observation of zero-quantum spin dynamics together with the coherence transfer pathway diagram.

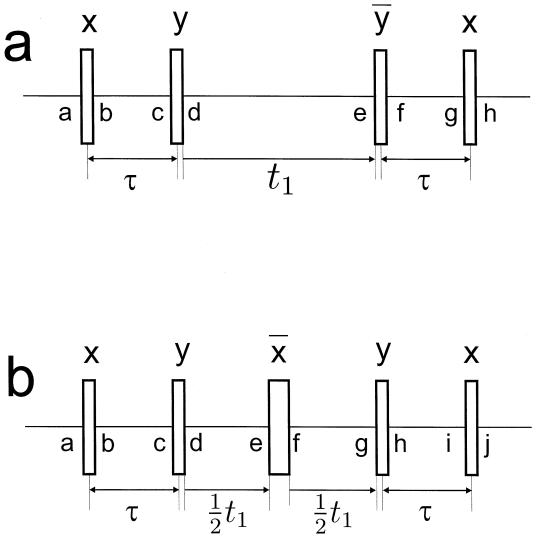

Fig. 6. Magnification of the central part of the pulse sequences in Fig. 5.

strong, non-selective $\pi/2$-pulses, separated by an interval τ. This sequence converts double-quantum coherence into zero-quantum coherence by generating a selective π rotation of one of the spins in each $^{13}C_2$ pair. For clarity, the relevant pulse sequence elements are displayed on an expanded scale in Fig. 6. The letters *a* to *h* refer to the timepoints in Fig. 6a.

If the density at time point ① is assumed to be proportional to the operator $S_{jz} + S_{kz}$, then the double-quantum part of the spin density operator directly after the $C7^{(+)}$ excitation block is

$$\rho^{DQ}(a) \simeq A\frac{1}{2}\left(e^{-i\phi}S_j^+ S_k^+ + e^{i\phi}S_j^- S_k^-\right) \tag{19}$$

where A is the amplitude of excited double-quantum coherence, and ϕ is the double-quantum phase. These parameters are given by

$$A = \sin\left(\left|\omega^{C7^{(+)}}\right|\tau_{exc}\right) \tag{20}$$

$$\phi = \phi_{C7}^{(+)} - \frac{\pi}{2} \tag{21}$$

where τ_{exc} is the duration of the first $C7^{(+)}$ block.

The effect of the two-pulse sequence may be written

$$U(d,a) = R_y\left(\frac{\pi}{2}\right)U^{free}(c,b)\,R_x\left(\frac{\pi}{2}\right) \tag{22}$$

where the pulse operators are

$$R_x\left(\frac{\pi}{2}\right) = \exp\left\{-i\frac{\pi}{2}S_x\right\} \tag{23}$$

$$R_y\left(\frac{\pi}{2}\right) = \exp\left\{-i\frac{\pi}{2}S_y\right\} \tag{24}$$

and $U^{\text{free}}(c,b)$ denotes the free precession propagator for the spin system over the time interval $b \Rightarrow c$.

If the dipole–dipole couplings and the CSA are neglected over the short interval τ, the pulse sequence propagator may be factorized

$$U(d,a) \simeq U_j(d,a)U_k(d,a) \tag{25}$$

where

$$U_j(d,a) \simeq R_y^j\left(\frac{\pi}{2}\right)R_z^j\left(\omega_j^{\text{iso}}\tau\right)R_x^j\left(\frac{\pi}{2}\right) \tag{26}$$

and

$$R_\mu^j(\beta) = \exp\left\{-i\beta S_\mu^j\right\} \tag{27}$$

Here, ω_j^{iso} is the isotropic shift frequency of spin j (relative to the spectrometer reference frequency), and S_μ^j is an angular momentum operator for spin j, with $\mu = x,y$ or z. Similar equations apply for spin k.

If the spectrometer reference frequency is set to the mean of the isotropic shift frequencies, then the chemically-shifted frequency offsets correspond to

$$\omega_j^{\text{iso}} = +\frac{1}{2}\omega_\Delta^{\text{iso}} \tag{28}$$

$$\omega_k^{\text{iso}} = -\frac{1}{2}\omega_\Delta^{\text{iso}} \tag{29}$$

where $\omega_\Delta^{\text{iso}} = \omega_j^{\text{iso}} - \omega_k^{\text{iso}}$.

If the free precession delay is set to $\tau = \pi/\omega_\Delta^{\text{iso}}$, then the individual spin propagators are given by

$$\begin{aligned} U_j(d,a) &\simeq R_y^j\left(\frac{\pi}{2}\right)R_z^j\left(\frac{\pi}{2}\right)R_x^j\left(\frac{\pi}{2}\right) \\ &= R_z^j\left(\frac{\pi}{2}\right)R_x^j(\pi) \end{aligned} \tag{30}$$

$$U_k(d,a) \simeq R_y^k\left(\frac{\pi}{2}\right)R_z^k\left(-\frac{\pi}{2}\right)R_x^k\left(\frac{\pi}{2}\right) = R_z^k\left(-\frac{\pi}{2}\right) \tag{31}$$

The effect of the two-pulse sequence upon the spin density operator at timepoint a may be deduced through the transformations

$$U_j(d,a)S_j^\pm U_j(d,a)^{-1} = \pm iS_j^\mp \tag{32}$$

$$U_k(d,a)S_k^\pm U_k(d,a)^{-1} = \pm iS_k^\pm \tag{33}$$

The zero-quantum part of the spin density operator at timepoint d is

$$\rho^{\text{ZQ}}(d) \simeq A\frac{1}{2}\left(-\mathrm{e}^{-i\phi}S_j^-S_k^+ - \mathrm{e}^{i\phi}S_j^+S_k^-\right) \tag{34}$$

This represents the conversion of double-quantum into zero-quantum coherence, with faithful transfer of the phase information.

3.2. Zero-quantum precession

The pulse sequence in Fig. 5a is appropriate for studies of the free precession of zero-quantum coherence. The zero-quantum coherence is allowed to precess freely for an interval t_1, and is then reconverted into observable signal by transfer back into double-quantum coherence, followed by conversion into longitudinal magnetization by a second C7 sequence.

The dynamics of zero-quantum coherences in rotating solids are complicated, especially in the vicinity of the rotational resonance condition [17,18], $\omega_\Delta^{\text{iso}} = n\omega_{\text{r}}$, where n is a small integer. At these conditions, zero-quantum coherence is interchanged with longitudinal difference magnetization in an oscillatory fashion.

In this paper, the experiments are performed well off rotational resonance, i.e., $|\omega_\Delta^{\text{iso}} - n\omega_{\text{r}}| \gg |\tilde{\omega}_{\text{B}}^{(n)}|$ for all n, where $\tilde{\omega}_{\text{B}}^{(n)}$ is the resonant part of the through space dipole–dipole coupling between spins S_j and S_k, as described in Ref. [17]. Under these conditions, the behavior of the zero-quantum coherence is relatively simple. If the homonuclear dipolar coupling is weak, the zero-quantum coherence oscillates at the frequency $\omega^{\text{ZQ}} \simeq \omega_\Delta^{\text{iso}}$, where $\omega_\Delta^{\text{iso}}$ is the isotropic shift frequency difference, and decays with the rate constant $R^{\text{ZQ}} = (T_2^{\text{ZQ}})^{-1}$.

In the case of strong homonuclear coupling between spin S_j and S_k, this simple picture must be

modified. A better approximation for the zero-quantum precession frequency is

$$\omega^{\mathrm{ZQ}} \simeq n\omega_{\mathrm{r}} + \left\{ \left(\omega_{\Delta}^{\mathrm{iso}} - n\omega_{\mathrm{r}} \right)^2 + \left| \tilde{\omega}_{\mathrm{B}}^{(n)} \right|^2 \right\}^{1/2} \qquad (35)$$

where n is the closest integer to $\omega_{\Delta}^{\mathrm{iso}}/\omega_{\mathrm{r}}$. The second term in Eq. (35) includes an off-resonant dipolar shift of the zero-quantum precession frequency. This term is orientation-dependent and causes inhomogeneous broadening of the zero-quantum spectrum, as described below. In addition to this shift, the zero-quantum precession occurs around a tilted effective field in the zero-quantum frame [18]. Although the tilt angle of the effective zero-quantum field is small if the experiment is conducted far from rotational resonance, there are still noticeable effects on the zero-quantum spin dynamics.

If the tilt of the zero-quantum effective field is ignored for simplicity, the zero-quantum spin density operator at timepoint e is given by

$$\begin{aligned} \rho^{\mathrm{ZQ}}(e) \simeq A\frac{1}{2}\Big[& \exp\left\{ i\left(\omega^{\mathrm{ZQ}} t_1 - \phi \right) \right\} S_j^- S_k^+ \\ & + \exp\left\{ -i\left(\omega^{\mathrm{ZQ}} t_1 - \phi \right) \right\} S_j^+ S_k^- \Big] \\ & \times \exp\left(-R^{\mathrm{ZQ}} t_1 \right) \end{aligned} \qquad (36)$$

3.2.1. Zero-quantum / double-quantum coherence transfer

After the evolution interval t_1, a further two-pulse sequence is applied between timepoints e and h (Fig. 6a). This sequence reconverts zero-quantum coherence into double-quantum coherence.

This sequence generates spin rotation operators with the following form:

$$U(h,e) \simeq U_j(h,e) U_k(h,e) \qquad (37)$$

where

$$\begin{aligned} U_j(h,e) &\simeq R_x^j\left(\frac{\pi}{2}\right) R_z^j\left(\frac{\pi}{2}\right) R_y^j\left(-\frac{\pi}{2}\right) \\ &= R_x^j(\pi)\, R_z^j\left(\frac{\pi}{2}\right) \end{aligned} \qquad (38)$$

$$\begin{aligned} U_k(h,e) &\simeq R_x^k\left(\frac{\pi}{2}\right) R_z^k\left(-\frac{\pi}{2}\right) R_y^k\left(-\frac{\pi}{2}\right) \\ &= R_z^k\left(-\frac{\pi}{2}\right) \end{aligned} \qquad (39)$$

These operators produce the transformations

$$U_j(h,e) S_j^{\pm} U_j(h,e)^{-1} = \mp i S_j^{\mp} \qquad (40)$$

$$U_k(h,e) S_k^{\pm} U_k(h,e)^{-1} = \pm i S_k^{\pm} \qquad (41)$$

The double-quantum part of the spin density operator at timepoint h is therefore

$$\begin{aligned} \rho^{\mathrm{DQ}}(h) = A\frac{1}{2}\Big[& \exp\left\{ i\left(\omega^{\mathrm{ZQ}} t_1 - \phi \right) \right\} S_j^+ S_k^+ \\ & + \exp\left\{ -i\left(\omega^{\mathrm{ZQ}} t_1 - \phi \right) \right\} S_j^- S_k^- \Big] \\ & \times \exp\left(-R^{\mathrm{ZQ}} t_1 \right) \end{aligned} \qquad (42)$$

In the case of no evolution interval $t_1 = 0$, the result is the same as in Eq. (19), i.e., directly after C7. Hence for $t_1 = 0$, the phases of the double-quantum coherence are restored in such a way that the second C7 sequence ($\mathrm{C7}^{(+)}$) reconverts the double-quantum coherences into observable magnetization, while avoiding destructive interference between the different orientational components.

For $t_1 \neq 0$, the zero-quantum coherences precess and causes a modulation of the NMR signal at the zero-quantum precession frequency, $\omega^{\mathrm{ZQ}} \simeq \omega_{\Delta}^{\mathrm{iso}}$.

3.3. Zero-quantum spectrum

Fig. 7a shows a two-dimensional spectrum obtained by the pulse sequence in Fig. 5a on [$^{13}C_2$,^{15}N]-glycine. A projection on the ω_1-axis is shown above the plot. The spinning frequency was $\omega_{\mathrm{r}}/2\pi = 5.000$ kHz and the decoupler field B^{I} corresponded to a ^{1}H nutation frequency $\omega_{\mathrm{nut}}^{\mathrm{I}}/2\pi = 90$ kHz. The spectrometer reference frequency was equal to the mean of the two isotropic shift frequencies. A complex FT was applied in the t_2-dimension, and a cosine FT in the t_1-dimension.

The phase cycling parameters were as in Eq. (12) with $n_1 = 1$, $n_2 = 1$, $n_3 = 4$, $n_4 = 1$, $n_5 = 4$, $n_6 = 4$, $n_7 = 1$, $n_{\mathrm{rec}} = 1$, $n_{\mathrm{tot}} = 64$. On each transient, the post digitization phase ϕ_{dig} was adjusted to satisfy the equation

$$\begin{aligned} & 2\phi_2 - 2\phi_3 + 2\phi_5 - 2\phi_6 - \phi_7 + \phi_{\mathrm{rec}} + \phi_{\mathrm{dig}} \\ & \quad = 2\phi_2^0 - 2\phi_3^0 + 2\phi_5^0 - 2\phi_6^0 - \phi_7^0 \end{aligned} \qquad (43)$$

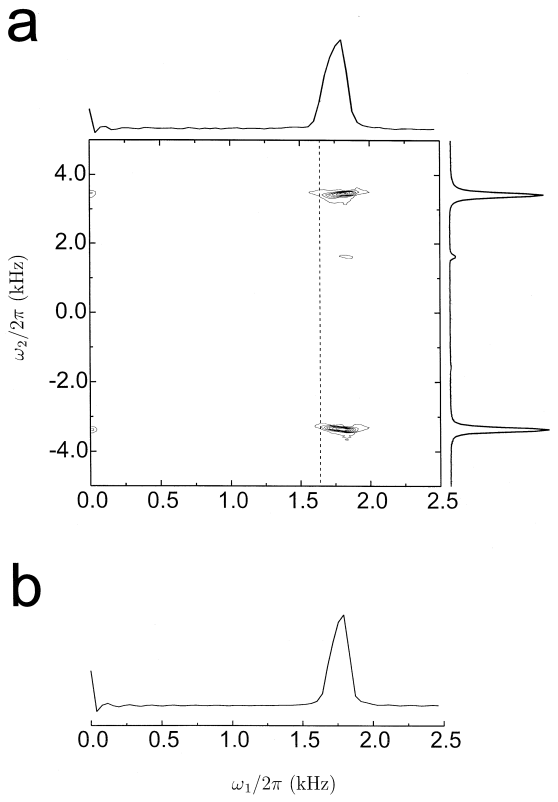

Fig. 7. (a) Two dimensional ^{13}C-spectrum obtained by the pulse sequence in Fig. 5a on [$^{13}C_2$,^{15}N]-glycine. The single-quantum dimension is ω_2, and the zero-quantum dimension is ω_1. The line graphs are projections of the signal-containing regions onto the frequency axes. The dashed line indicates the expected zero-quantum frequency, neglecting dipolar shifts (see text). (b) A spin dynamical simulation of the ω_1-projection.

where the initial phases for the phase cycle were

$$\phi_1^0 = \phi_2^0 = \phi_3^0 = \phi_4^0 = \phi_5^0 = \phi_7^0 = 0 \tag{44}$$

$$\phi_6^0 = \frac{1}{2}\omega_r\left(t_{②} - t_{①}\right) + \frac{\pi}{2} \tag{45}$$

and the timepoints $t_{①}$ and $t_{②}$ are indicated in Fig. 5.

The spectrum displays prominent zero-quantum peaks at the frequency coordinate $\omega_1/2\pi \simeq 1800$ Hz. These peaks do not appear exactly at the isotropic shift frequency difference $\omega_\Delta^{iso}/2\pi = 6620$ Hz, whose position is indicated by the dotted line, after taking into account folding caused by the restricted spectral bandwidth in the ω_1 dimension, which was 5000 Hz. There are also small peaks at $\omega_1 = 0$.

The broadening and shift of the zero-quantum peaks are both due to the strong homonuclear ^{13}C–^{13}C couplings in this compound. The precession of the zero-quantum coherences around a tilted effective field causes small signals at $\omega_1 = 0$.

A spin dynamical simulation of the experiment yields the two-dimensional spectral projection shown in Fig. 7b. This simulation was performed using the methods described in Ref. [18]. The shift and the broadening of the experimental zero-quantum spectrum, as well as the $\omega_1 = 0$ peaks, are well reproduced in the simulation.

Because of these inhomogeneous dipolar shifts, the pulse sequence in Fig. 6a cannot be used for measurement of the zero-quantum decay rate constant R^{ZQ}.

3.4. Decay of zero-quantum coherence: measurement of T_2^{ZQ}

In Fig. 5b, a π-pulse is inserted in the middle of the zero-quantum evolution interval t_1. The π-pulse refocuses the inhomogeneous dipolar shifts of the zero-quantum peaks, and allows a more straightforward estimate of the zero-quantum decay rate constant R^{ZQ}.

Consider the first two pulses in the expanded diagram of Fig. 6b. From timepoint *a* to timepoint *d*, the sequence is identical to that in Fig. 6a.

At timepoint *e*, the zero-quantum part of the density operator is given by

$$\rho^{ZQ}(e) \simeq A\frac{1}{2}\left[-\exp\left\{i\left(\omega^{ZQ}\frac{t_1}{2} - \phi\right)\right\}S_j^- S_k^+ + \exp\left\{-i\left(\omega^{ZQ}\frac{t_1}{2} - \phi\right)\right\}S_j^+ S_k^-\right] \times \exp\left\{-\frac{1}{2}R^{ZQ}t_1\right\} \tag{46}$$

if the tilt of the zero-quantum effective field is ignored.

The effect of the π-pulse may be written

$$R_x(\pi)S_j^{\mp}S_k^{\pm}R_x(\pi)^{-1} = S_j^{\pm}S_k^{\mp} \tag{47}$$

and hence

$$\rho^{ZQ}(f) \simeq A\frac{1}{2}\left[\exp\left[-i\left(\omega^{ZQ}\frac{t_1}{2}-\phi\right)\right]S_j^- S_k^+ + \exp\left[i\left(\omega^{ZQ}\frac{t_1}{2}-\phi\right)\right]S_j^+ S_k^-\right] \times \exp\left\{-\frac{1}{2}R^{ZQ}t_1\right\} \quad (48)$$

This indicates that the π-pulse changes the phase of the zero-quantum coherence. This phase change must be compensated by the last two-pulse sequence in order to obtain a finite signal in a powder.

Precession of the zero-quantum coherence in the interval f to g gives a zero-quantum spin density operator of the form

$$\rho^{ZQ}(g) \simeq A\frac{1}{2}\left(e^{i\phi}S_j^- S_k^+ + e^{-i\phi}S_j^+ S_k^-\right) \times \exp\left\{-R^{ZQ}t_1\right\} \quad (49)$$

which is now independent of the inhomogeneous zero-quantum precession frequency ω^{ZQ}.

The final two pulse sequence produces spin rotation operators with the following form

$$U_j(j,g) \simeq R_x^j\left(\frac{\pi}{2}\right)R_z^j\left(\frac{\pi}{2}\right)R_y^j\left(\frac{\pi}{2}\right) = R_z^j\left(\frac{\pi}{2}\right) \quad (50)$$

$$U_k(j,g) \simeq R_x^k\left(\frac{\pi}{2}\right)R_z^k\left(-\frac{\pi}{2}\right)R_y^k\left(\frac{\pi}{2}\right) = R_x^k(\pi)\,R_z^k\left(-\frac{\pi}{2}\right) \quad (51)$$

This sequence leads to the following transformations:

$$U_j(j,g)\,S_j^{\pm}\,U_j(j,g)^{-1} = \pm iS_j^{\pm} \quad (52)$$

$$U_k(j,g)\,S_k^{\pm}\,U_k(j,g)^{-1} = \pm iS_k^{\mp} \quad (53)$$

The double-quantum density operator at timepoint j is therefore

$$\rho^{DQ}(j) \simeq A\frac{1}{2}\left(e^{-i\phi}S_j^+ S_k^+ + e^{+i\phi}S_j^- S_k^-\right) \times \exp\left\{-R^{ZQ}t_1\right\} \quad (54)$$

This result is the same as at timepoint a in Eq. (19), except for the zero-quantum decay factor. This ensures that the last C7 sequence reconverts double-quantum coherence into observable signal, without destructive interference between the orientational components. The zero-quantum decay constant R^{ZQ} may be estimated by conducting a series of experiments with different values of the evolution interval t_1.

3.4.1. [11,20-$^{13}C_2$]-all-E-retinal

Fig. 8a shows experimental points (circles) for the labelled retinal, obtained with the pulse sequence in Fig. 5b. The experiment was performed at a decoupler level B^I corresponding to a proton nutation frequency of 90 kHz, and a sample spinning frequency of 4.5 kHz. Each point represent the sum of the spectral peak integrals as a function of evolution interval t_1.

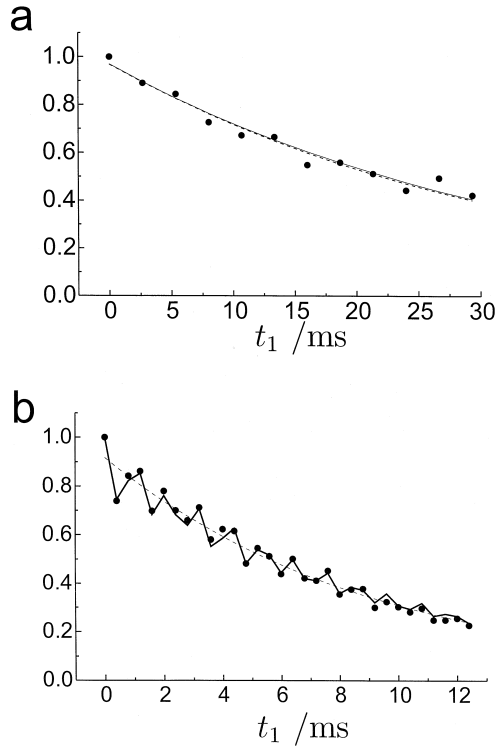

Fig. 8. Zero-quantum decay for (a) [11,20-$^{13}C_2$]-retinal and (b) [$^{13}C_2$, ^{15}N]-glycine. The filled circles denote the sum of the integrated area under the two spectral peaks at indicated evolution intervals t_1, normalized so that the first point in each series is equal to 1.0. The solid lines are the result of accurate numerical simulations. The dashed lines are best fits to exponential decays.

The phase cycling parameters were as in Eq. (12) with $n_1 = 1$, $n_2 = 1$, $n_3 = 4$, $n_4 = 1$, $n_5 = 4$, $n_6 = 4$, $n_7 = 1$, $n_{\mathrm{rec}} = 1$, $n_{\mathrm{tot}} = 64$. On each transient, the post digitization phase ϕ_{dig} was adjusted to satisfy the equation

$$+2\phi_2 - 2\phi_3 + 2\phi_5 - 2\phi_6 - \phi_7 + \phi_{\mathrm{rec}} + \phi_{\mathrm{dig}} = 2\phi_2^0 - 2\phi_3^0 + 2\phi_5^0 - 2\phi_6^0 - \phi_7^0 \quad (55)$$

with initial phases given by

$$\phi_1^0 = \phi_2^0 = \phi_3^0 = \phi_4^0 = \phi_5^0 = \phi_7^0 = 0 \quad (56)$$

$$\phi_6^0 = \frac{1}{2}\omega_r \left(t_{②} - t_{①}\right) + \frac{\pi}{2} \quad (57)$$

The results in Fig. 8a display a rather slow, monotonic damping of the zero-quantum coherence.

The dashed line is the best fit of these experimental points to an exponential decay. This leads to an estimate of the zero-quantum decay rate constant $R^{\mathrm{ZQ}} = 31 \pm 2\ \mathrm{s}^{-1}$, corresponding to a zero-quantum relaxation time constant $T_2^{\mathrm{ZQ}} = 32 \pm 2$ ms.

The solid line is a simulated curve of the zero-quantum spin dynamics, using the methods described in Ref. [18]. The zero-quantum decay rate constant $R^{\mathrm{ZQ}} = 31\ \mathrm{s}^{-1}$ was used. The simulated curve coincides almost exactly with the exponential decay curve (dashed line). The spin interaction parameters are given below.

3.4.2. [$^{13}C_2$,^{15}N]-glycine

Fig. 8b shows experimental points (circles) for [$^{13}C_2$,^{15}N]-glycine. The experiment was performed at a decoupler level B^I corresponding to a proton nutation frequency of 90 kHz, and a sample spinning frequency $\omega_r/2\pi = 5.000$ kHz. The phase cycling parameters were as given in Eqs. (55)–(57).

The experimental points show oscillations of signal amplitude as a function of t_1. These oscillations are due to zero-quantum precession about a tilted effective field, in the case of strong homonuclear ^{13}C–^{13}C couplings, as described above. A simulation of the experiment reproduces these oscillations rather well (solid line). This simulation assumed an initial zero-quantum spin density operator given by Eq. (34), with double-quantum phases specified in Eqs. (21) and (5). The form of the oscillations proved to be sensitive to the initial phase of the zero-quantum coherences.

The decay rate constant of the zero-quantum coherences, as determined by accurate spin dynamical simulations, is $R^{\mathrm{ZQ}} = 111 \pm 2\ \mathrm{s}^{-1}$. A similar result is obtained by simply fitting the experimental points to an exponential decay ($R^{\mathrm{ZQ}} = 108 \pm 5\ \mathrm{s}^{-1}$).

4. Decay of single-quantum coherence

We also measured single-quantum decay rate constants by using Hahn echo pulse sequences to compensate for static magnetic field inhomogeneities [33]. Instead of using a strong non-selective π-pulse, we employed the two-pulse selective inversion sequences discussed above. The selective π-rotation on one of the spin sites ensures that isotropic *J*-coupling and off-resonant dipolar shifts are both refocused.

The appropriate pulse sequences are shown in Fig. 9. The spectrometer reference frequency is set to the mean of the two isotropic chemical shift frequencies. *S*-spin transverse magnetization is created by ramped cross-polarization from the ^{1}H-spins. The

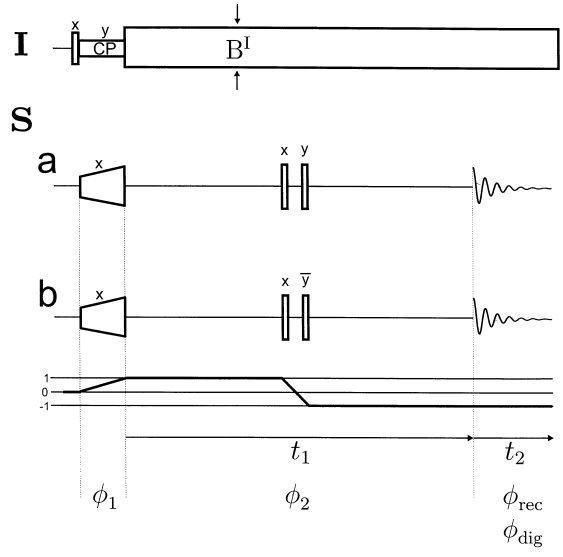

Fig. 9. Pulse sequence for investigation of single-quantum coherence decay. The delay τ is equal to $\tau = \pi / \omega_\Delta^{\mathrm{iso}}$, where $\omega_\Delta^{\mathrm{iso}} = \omega_j^{\mathrm{iso}} - \omega_k^{\mathrm{iso}}$ is the isotropic chemical shift frequency difference. Scheme (a) is used for measuring the single-quantum coherence decay of the most-shielded site. Scheme (b) is used for measuring the single-quantum coherence decay of the least-shielded site.

single quantum coherences are allowed to precess for an interval $1/2t_1$, chosen to be an integer multiple of the rotor period $\tau_r = 2\pi/\omega_r$. The two-pulse sequence is applied, followed by a further interval $1/2t_1$. The decay curve of single-quantum coherence is obtained by incrementing the t_1-interval, keeping the two-pulse sequence in the middle, and measuring the area under the appropriate spectral peak as a function of t_1. The decay curve is fitted to a single exponential function to yield the relaxation time constant T_{2j}^{SQ}, where j is the spin site which is selectively inverted. The experiment is repeated with different phases of the two-pulse sequence in order to measure the decay of the other spectral peak k. If the two-pulse sequence has the form $(\pi/2)_x - \tau - (\pi/2)_y$ (scheme a in the figure), where $\tau = \pi/\omega_\Delta^{iso}$, then the most-shielded site j is inverted; if the two-pulse sequence has the form $(\pi/2)_x - \tau - (\pi/2)_{\bar{y}}$, then the least-shielded site k is inverted (scheme b in the figure).

Correct operation of these sequences requires careful attention to the signs of the radio-frequency phases. One must take into account the sign of the Larmor frequency as well as the rf mixing pathway in the spectrometer console (see Ref. [29] and Section 5).

4.1. [11,20-$^{13}C_2$]-all-E-retinal

Fig. 10a shows experimental points (symbols) for the labelled retinal obtained with the pulse sequence in Fig. 9.

Each point represent the relevant spectral peak integral as a function of evolution interval t_1. The experiment was performed at a sample rotation frequency of $\omega_r/2\pi = 4.500$ kHz and a decoupler field B^I corresponding to a proton nutation frequency of 90 kHz.

The following four-step phase cycle was used to select the CTP indicated in Fig. 9:

$$\phi_1 = 0 \quad (58)$$

$$\phi_2 = \phi_{rec} = \phi_{dig} = \pi m/2 \quad (59)$$

where m is the transient counter.

The estimated decay rate constant for the 11-^{13}C-site was $R_k^{SQ} = 20 \pm 2\ s^{-1}$ corresponding to a relaxation time constant of $T_{2k}^{SQ} = 49 \pm 4$ ms (dashed line). The corresponding figures for the 20-^{13}C-site were $R_j^{SQ} = 15 \pm 3\ s^{-1}$ and $T_{2j}^{SQ} = 69 \pm 5$ ms (solid line).

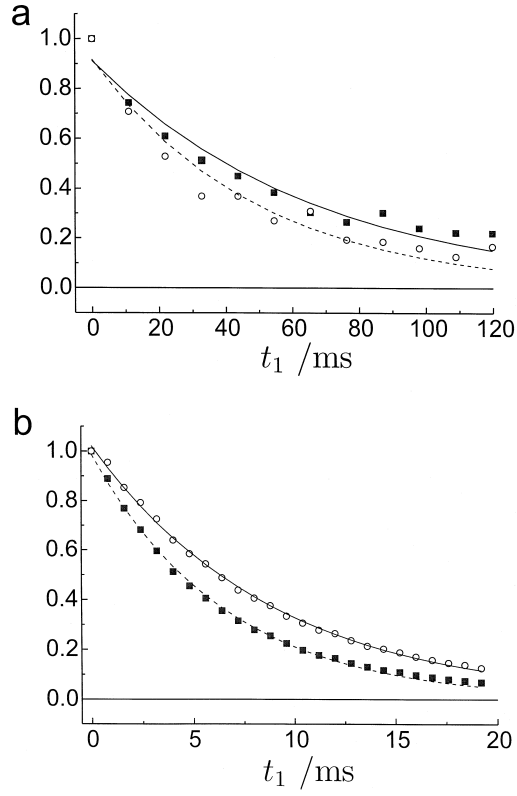

Fig. 10. Single-quantum decay for (a) [11,20-$^{13}C_2$]-retinal and (b) [$^{13}C_2$,^{15}N]-glycine. In (a), the filled squares denote the 20-^{13}C-site and open circles the 11-^{13}C-site. In (b), the filled squares denote the methylene (2-^{13}C) site and open circles the carboxyl (1-^{13}C) site. Each series is normalized so that the first point is equal to 1.0. The lines are best fits of the experimental data to exponential decays.

4.2. [$^{13}C_2$,^{15}N]-glycine

Fig. 10b shows experimental points (symbols) for the labelled glycine sample obtained with the pulse sequence in Fig. 9.

Each point represents the relevant spectral peak integral as a function of evolution interval t_1. The experiment was performed at a sample rotation frequency of $\omega_r/2\pi = 5.000$ kHz and a decoupler field B^I corresponding to a proton nutation frequency of

90 kHz. The phase cycling was the same as in the retinal experiment.

The measured single-quantum decay rate constants for [$^{13}C_2$,^{15}N]-glycine were for the carboxyl site, $R_k^{SQ} = 113 \pm 2\ s^{-1}$ corresponding to a relaxation time constant of $T_{2k}^{SQ} = 8.82 \pm 0.08$ ms (solid line). The corresponding figures for the methylene site were $R_j^{SQ} = 154 \pm 2\ s^{-1}$ and $T_{2j}^{SQ} = 6.49 \pm 0.08$ ms (dashed line).

5. Experimental

5.1. Samples

[11,20-$^{13}C_2$]-all-*E*-retinal was synthesized as described in Ref. [34]. The labeled retinal was re-crystallized from liquid n-pentane with a nine-fold excess of natural abundance retinal (Fluka, Switzerland) at -80°C. Approximately 60 mg of the 10%-[11,20-$^{13}C_2$]-all-*E*-retinal was packed in a Chemagnetics zirconium oxide rotor with outer diameter 4 mm.

[$^{13}C_2$,^{15}N]-glycine (98% ^{13}C, 96–99% ^{15}N) was purchased from Cambridge Isotopes and used without further purification or dilution. Approximately 59 mg was packed in a Chemagnetics zirconium oxide rotor with outer diameter 4 mm.

5.2. Experiments

All experiments was performed on a Chemagnetics CMX-200 spectrometer operating at a magnetic field of 4.7 T. A Chemagnetics triple-resonance MAS probe with a 4 mm spinner module was used. The spinning frequency was stabilized to ± 2 Hz.

In all experiments, the cross-polarization interval was equal to 2.0 ms. The ^{13}C rf-field intensity during cross-polarization was ramped to increase reproducibility [25]. The ^{1}H $\pi/2$-pulse duration was between 5.2 and 5.9 μs.

In the experiments on [11,20-$^{13}C_2$]-retinal, the ^{13}C-field during the C7 sequence corresponded to a *S*-spin nutation frequency of $\omega_{nut}^{S}/2\pi = 35$ kHz. The C7 excitation sequence employed 50 rf cycles with a total excitation interval $\tau_{exc} = 3.175$ ms.

In the experiments on [$^{13}C_2$,^{15}N]-glycine, the rf-field on the ^{13}C-spins during C7 corresponded to a *S*-spin nutation frequency $\omega_{nut}^{S}/2\pi = 32.8$ kHz. The C7 excitation sequence employed 10 rf-cycles, occupying a total excitation interval $\tau_{exc} = 571$ μs.

In all pulse sequences, the indicated phases denote nutation axis phases of the spins. Care has to be taken to implement these phases with the correct sign in the pulse programmer, as discussed in Ref. [29]. On our CMX-200 console, the rf synthesizer phases coincide with the nutation axis phases of the spins, due to two consecutive sign changes: the first due to a down-conversion of a 283 MHz intermediate frequency signal; the second due to the negative sign of the Larmor frequency.

5.3. Simulations

The simulation on [11,20-$^{13}C_2$]-all-*E*-retinal employed the following parameters [4]: shift anisotropy δ_k^{aniso} and asymmetry parameter η_k for the 11-^{13}C-site: 112.2 ppm and 0.72. Shift anisotropy δ_j^{aniso} and asymmetry parameter η_j for the 20-^{13}C-site: 15.5 ppm and 1.0. Isotropic shift difference $\delta_k^{iso} - \delta_j^{iso} = 121.2$ ppm (Deshielding convention used throughout). Through space dipolar coupling $b_{jk}/2\pi = -293$ Hz, corresponding to an internuclear distance $r = 0.296$ nm [35]. The molecules frame M was chosen so that the *z*-axis was along the internuclear vector; the principal axis frames of the 11-^{13}C- and the 20-^{13}C-site shift tensors were oriented at angles $\Omega_k^{PM} = \{-31°, 85°, -87°\}$ and $\Omega_j^{PM} = \{0, 57°, 0\}$ with respect to the molecule fixed frame [5]. The three bond ^{13}C–^{13}C isotropic *J*-coupling was ignored.

The simulation on [$^{13}C_2$,^{15}N]-glycine employed the following parameters [36]: for the ^{13}COO-site: shift anisotropy $\delta_k^{aniso} = -74.5$ ppm and asymmetry parameter $\eta_k = 0.88$. For the $^{13}CH_2$-site: shift anisotropy $\delta_j^{aniso} = -19.43$ ppm and asymmetry parameter $\eta_j = 0.98$. Isotropic shift difference $\delta_j^{iso} - \delta_k^{iso} = 130$ ppm. Through space dipolar coupling $b_{jk}/2\pi = -2135$ Hz, corresponding to an internuclear distance $r = 0.1526$ nm [37]. A molecule fixed frame M with a *z*-axis along the internuclear vector was chosen; the principal axis frame of the carboxyl and the methylene shift tensors were oriented at angles $\Omega_k^{PM} = \{-0.7°, 88.5°, 42.5°\}$ and $\Omega_j^{PM} =$

{99.4°,146.0°,138.9°} with respect to the molecule fixed frame. The isotropic *J*-coupling was $J_{jk} = 53.1$ Hz [36].

6. Discussion

The URF model may be tested by comparing the predictions of Eq. (1) with experimental results. For the case of 10%-[11,20-$^{13}C_2$]-all-*E*-retinal, the measured decay rate constants were $R^{ZQ} = 31 \pm 2\ s^{-1}$, $R^{DQ} = 29 \pm 2$, $R_j^{SQ} = 15 \pm 3\ s^{-1}$, $R_k^{SQ} = 20 \pm 2\ s^{-1}$, obtained under identical experimental conditions. These are reasonably consistent with the URF model. In particular, the measured zero and double-quantum rate constants are in good mutual agreement. The sum of the single-quantum rate constants $R_j^{SQ} + R_k^{SQ} = 35 \pm 5\ s^{-1}$, is also in reasonable agreement with the double- and zero-quantum rate constants. This supports the idea that the URF model is rather well applicable to ^{13}C spins separated by rather long distances (0.297 nm in the present case).

In the case of 98%-[$^{13}C_2$,^{15}N]-glycine, we obtain the multiple-quantum decay rate constants $R^{ZQ} = 111 \pm 2\ s^{-1}$ and $R^{DQ} = 197 \pm 2\ s^{-1}$. The measured single-quantum rate constants for the glycine sample were $R_j^{SQ} = 154 \pm 2\ s^{-1}$ for the methylene site and $R_k^{SQ} = 113 \pm 2\ s^{-1}$ for the carboxyl site. These figures are inconsistent with the URF model. The discrepancy may be connected to correlations in the random fields, as well as the strong intermolecular homonuclear couplings in this non-diluted compound.

Future experiments are planned on isotopically-diluted labelled glycine samples, in order to investigate further the mechanism of the deviations from the URF model.

In conclusion, the measured relaxation rate constants for ^{13}C spin pairs in rotating solids support the validity of the URF model at rather long ^{13}C–^{13}C distances. This result is of immediate relevance to molecular structural studies by rotational resonance.

The URF model is in clear discrepancy with experiments in the case of [$^{13}C_2$,^{15}N]-glycine. Fortunately, the estimation of internuclear distances by rotational resonance is very insensitive to the assumed relaxation behavior in the case of short ^{13}C–^{13}C distances.

Acknowledgements

The Swedish National Science Foundation and the Göran Gustafsson Foundation for Research in the Natural Sciences and Medicine are acknowledged for supporting this research. The authors thank Ole G. Johanessen for technical assistance, and Mattias Edén for discussions.

References

[1] F. Creuzet, A. McDermott, R. Gebhardt, K. van der Hoef, M.B. Spijker-Assink, J. Herzfeld, J. Lugtenburg, M.H. Levitt, R.G. Griffin, Science 251 (1991) 783–786.
[2] O.B. Peersen, S. Yoshimura, H. Hojo, S. Aimoto, S.O. Smith, J. Am. Chem. Soc. 114 (1992) 4332–4335.
[3] D.R. Studelska, C.A. Klug, D.D. Beusen, L.M. McDowell, J. Schaefer, J. Am. Chem. Soc. 118 (1996) 5476–5477.
[4] P.J.E. Verdegem, M. Helmle, J. Lugtenburg, H.J.M. de Groot, J. Am. Chem. Soc. 119 (1997) 169–174.
[5] X. Feng, P.J.E. Verdegem, Y.K. Lee, M. Helmle, S.C. Shekar, H.J.M. de Groot, J. Lugtenburg, M.H. Levitt, in manuscript.
[6] D.M. Gregory, M.A. Mehta, J.C. Shiels, G.P. Drobny, J. Chem. Phys. 107 (1997) 28–42.
[7] A.E. McDermott, F. Creuzet, R. Gebhard, K. Van der Hoef, M.H. Levitt, J. Herzfeld, J. Lugtenburg, R.G. Griffin, Biochemistry 33 (1994) 6129–6136.
[8] K. Schmidt-Rohr, J. Am. Chem. Soc. 118 (1996) 7601–7603.
[9] X. Feng, Y.K. Lee, D. Sandström, M. Edén, H. Maisel, A. Sebald, M.H. Levitt, Chem. Phys. Lett. 257 (1996) 314–320.
[10] X. Feng, M. Edén, A. Brinkmann, H. Luthman, L. Eriksson, A. Gräslund, O.N. Antzutkin, M.H. Levitt, J. Am. Chem. Soc. 119 (1997) 12006–12007.
[11] X. Feng, P.J.E. Verdegem, Y.K. Lee, D. Sandström, M. Edén, P. Bovee-Geurts, W.J. de Grip, J. Lugtenburg, H.J.M. de Groot, M.H. Levitt, J. Am. Chem. Soc. 119 (1997) 6853–6857.
[12] M. Hong, J.D. Gross, R.G. Griffin, J. Phys. Chem. B 101 (1997) 5869–5874.
[13] P.R. Costa, J.D. Gross, M. Hong, R.G. Griffin, Chem. Phys. Lett. 280 (1997) 95–103.
[14] Y. Ishii, T. Terao, M. Kainosho, Chem. Phys. Lett. 256 (1996) 133–140.
[15] E.R. Andrew, A. Bradbury, R.G. Eades, V.T. Wynn, Phys. Lett. 4 (1963) 99–100.
[16] D.P. Raleigh, M.H. Levitt, R.G. Griffin, Chem. Phys. Lett. 146 (1988) 71–76.
[17] M.H. Levitt, D.P. Raleigh, F. Creuzet, R.G. Griffin, J. Chem. Phys. 92 (1990) 6347–6364.
[18] T. Karlsson, M.H. Levitt, J. Chem. Phys. 109 (1998) 5493–5507.
[19] A. Kubo, C.A.J. McDowell, Chem. Soc. Faraday Trans. 1 84 (1988) 3713–3730.

[20] M.M. Maricq, J.S. Waugh, J. Chem. Phys. 70 (1979) 3300–3316.
[21] D.L. VanderHart, G.C. Campbell, J. Magn. Res. 134 (1998) 88–112.
[22] K. Eichele, M.D. Lumsden, R.E. Wasylishen, J. Phys. Chem. 97 (1993) 8909–8916.
[23] R.R. Ernst, G. Bodenhausen, A. Wokaun, Principles of Nuclear Magnetic Resonance in One and Two Dimensions, Clarendon Press, Oxford, 1987.
[24] A. Pines, M.G. Gibby, J.S. Waugh, J. Chem. Phys. 56 (1972) 1776–1777.
[25] G. Metz, X. Wu, S.O. Smith, J. Magn. Res. A 110 (1994) 219–227.
[26] Y.K. Lee, N.D. Kurur, M. Helmle, O.G. Johannessen, N.C. Nielsen, M.H. Levitt, Chem. Phys. Lett. 242 (1995) 304–309.
[27] M. Hohwy, H.J. Jakobsen, M. Edén, M.H. Levitt, N.C. Nielsen, J. Chem. Phys. 108 (1998) 2686–2694.
[28] C.M. Rienstra, M.E. Hatcher, L.J. Mueller, B. Sun, S.W. Fesik, R.G. Griffin, J. Am. Chem. Soc. 120 (1998) 10602–10612.
[29] M.H. Levitt, J. Magn. Res. 126 (1997) 164–182.
[30] A. Brinkmann, M. Edén, M.H. Levitt, in preparation.
[31] W.A. Dollase, M. Feike, H. Förster, T. Schaller, I. Schnell, A. Sebald, S. Steuernagel, J. Am. Chem. Soc. 119 (1997) 3807–3810.
[32] M. Baldus, M. Tomaselli, B.H. Meier, R.R. Ernst, Chem. Phys. Lett. 230 (1994) 329–336.
[33] E.L. Hahn, Phys. Rev. 80 (1950) 580–594.
[34] M. Groesbeek, J. Lugtenburg, Photochem. Photobiol. 56 (1992) 903–908.
[35] T. Hamanaka, T. Mitsui, T. Ashida, M. Kakudo, Acta Cryst. B 28 (1972) 214–222.
[36] R.A. Haberkorn, R.E. Stark, H. van Willigen, R.G. Griffin, J. Am. Chem. Soc. 102 (1981) 2534–2539.
[37] P.-G. Jönsson, Å. Kvick, Acta Cryst. B 28 (1972) 1827–1833.